

Microfluidic Shrinking Droplet Concentrator for Analyte Detection and Phase Separation of Protein Solutions

Marie R. G. Kopp, Miriam Linsenmeier, Britta Hettich, Sebastian Prantl, Stavros Stavrakis, Jean-Christophe Leroux, and Paolo Arosio*



Cite This: *Anal. Chem.* 2020, 92, 5803–5812



Read Online

ACCESS |



Metrics & More

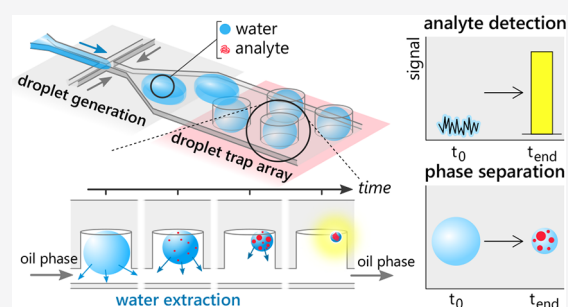


Article Recommendations



Supporting Information

ABSTRACT: We develop a droplet microfluidic platform to increase the concentration of analytes in solution via reduction of the sample volume under well-defined conditions. This approach improves the detection and quantification of analytes without requiring any *a priori* information on their structure nor physical chemical properties. Samples are compartmentalized and processed in water-in-oil droplets that are individually stored in cylindrical microwells located on top of a microfluidic channel. The individual droplets shrink over time due to water extraction in the surrounding oil, leading to an increase in the analyte concentration up to 100,000-fold within the droplet. We demonstrate the power of this approach for detection applications by quantifying a broad range of single analytes such as small molecules, proteins, nanoparticles, exosomes, and amyloid fibrils. With this setup, we can measure pM concentrations, corresponding to zeptomole (10^{-21} mol) amounts encapsulated in individual droplets. We further show that the droplet concentrator device, or DroMiCo, can quantify unlabeled proteins in nM concentrations and analyze multicomponent mixtures when coupled with a prefractionation step. We illustrate this concept by detecting femtomoles (10^{-15} mol) of soluble protein oligomers prefractionated by size exclusion chromatography. Finally, we apply the DroMiCo to the analysis of phase diagrams of macromolecules, including synthetic polymers and proteins. Specifically, we analyze the liquid–liquid phase separation of an *in vitro* model of cellular membraneless compartments, composed of a phase separating protein in the presence of defined concentrations of molecular modulators such as RNA and ATP.



The quantification of tiny amounts of molecular species is a ubiquitous problem in chemical and biological assays. Common strategies rely on immuno- and enzyme-based assays (e.g., ELISA), on the amplification of the number of molecules, as in the case of polymerase chain reaction (PCR) of nucleic acids, or on a combination of these techniques. However, these methods may be difficult to implement if structural information is missing, if samples are heterogeneous mixtures, or if the analyte cannot be amplified, as in the case of protein aggregates,^{1–4} vesicles,^{5,6} and other particles.

Another common strategy relies on increasing the sensitivity of optical detection methods, such as UV absorption and fluorescence spectroscopies, by enhancing the signal-to-noise ratio, for instance by locally concentrating the analyte.^{7,8} In this context, microfluidic platforms represent attractive tools to manipulate and concentrate molecules in defined positions,^{9–11} as they offer superior control on the analyte microenvironment compared to bulk methods.^{12,13} Current lithography techniques allow designing geometries at the micrometer and nanometer scales, enabling one to create physical restrictions on a scale comparable to the size of cells¹⁴ and macromolecules.¹⁵ The manipulation and concentration of molecules are actively or passively controlled by integrating the microfluidic channels with electric fields, acoustic wave fields, porous membranes, and

surface chemistry techniques, thereby leading to the development of microfluidic concentration devices based on electrophoresis^{16,17} and electro-kinetic traps,^{18–22} acoustic trapping,²³ passive size separation,^{24–26} and affinity chromatography^{16,27–30}, respectively. As a result, microfluidic concentrator devices have found several successful applications in the detection of biomolecules and the enhancement of reaction kinetics.^{18,31–33} However, some approaches require challenging fabrication techniques, and most concentration processes depend on the physical-chemical properties of the analytes such as charge, size, and specific interactions, for example with a specific reagent or matrix of the stationary phase. These aspects can require a tailored design of the components of the microfluidic device, complex operation procedures, as well as expensive reagents.

Received: November 25, 2019

Accepted: March 17, 2020

Published: April 6, 2020



An attractive alternative offered by droplet microfluidics relies on the confinement of solutions in well-defined water-in-oil microcompartments, which can be stored in suitable chambers.^{34–38} The decrease in droplet volume over time due to the evaporation of water molecules increases the analyte concentration in the droplet, therefore amplifying its signal. This technique allows one to measure analyte samples ranging from small molecules to biomacromolecules and colloids, independently of their physical-chemical properties.^{37–40} This concept has been demonstrated with different configurations, ranging from sessile droplets^{39,40} to trapping of water-in-oil emulsions in PDMS devices.^{34,35,41} Here, we develop a novel configuration in which droplets are trapped inside microwells located on top of the microfluidic channel that follows the droplet generator. In our configuration, the droplets remain trapped even upon severe shrinkage, from a few nL to a few fL, and maintain a spherical shape during the entire process, therefore allowing the accurate measurement of the droplet volume and unknown analyte concentration. The latter is evaluated by measuring the number of molecules inside the droplets and the known volume of the initial droplets. The opportunity to measure large numbers of different individual droplets generates high statistics, thereby leading to a robust evaluation of the number of molecules inside the droplets. Significant advantages of the assay arise from the fact that the technique does not require any *a priori* information on the structure nor physical-chemical properties of the analytes.

We demonstrate the potential of our shrinking droplet microfluidic concentrator assay (DroMiCo) with a broad range of single target analytes in simple media, including small molecules, proteins, nanoparticles, exosomes, and amyloid fibrils. Additionally, we demonstrate that our setup enables the detection and quantification of unlabeled proteins down to 100 nM, thereby improving the detection sensitivity of conventional techniques such as the bicinchoninic acid (BCA)⁴² or Bradford assays⁴³ by one order of magnitude. As one potential application, we demonstrate the ability of the DroMiCo to detect tiny amounts of individual target species isolated from a multicomponent mixture by size exclusion chromatography.

We further apply the DroMiCo to the analysis of phase diagrams of macromolecules, based on the ability of the DroMiCo to increase their concentrations by removing water molecules. We illustrate this concept with two model systems, namely the liquid–liquid phase separation of poly(ethylene glycol) (PEG) molecules in the presence of ammonium sulfate and the precipitation of lysozyme in the presence of sodium chloride. We also investigate a solution of increased complexity, representing an *in vitro* model of cellular membraneless organelles. Specifically, we study an established model of processing bodies consisting of the phase separation of the DEAD-box protein ATPase Dhh1 in the presence of ATP and RNA.^{44,45} The formation of membraneless compartments in cells via liquid–liquid phase separation of proteins and nucleic acids is emerging as a key process in a variety of cellular functions and dysfunctions.^{46–48} Yet, several questions about the molecular determinants of this process are still open.^{45,48,49} In this context, the shrinking process in the DroMiCo allows one to observe in real time the phase separation upon the increase in protein concentration, starting from a homogeneous solution at subcritical concentrations and reaching supersaturation during shrinkage of the droplets. Moreover, due to the high concentration factor, the DroMiCo covers a broad range of concentrations, including high concentration of biomolecules

typically not accessible in bulk assays, while requiring minute amounts of material.

MATERIALS AND METHODS

Fluorophores. The fluorescent dye ATTO-TEC 488 (A488, NHS ester) was purchased from ATTO-TEC GmbH (Germany) and stored as a 2 g/L solution in dimethyl sulfoxide (DMSO, Sigma-Aldrich, Germany) at $-20\text{ }^{\circ}\text{C}$. Samples at known concentration were prepared by serial dilutions in Milli-Q water (Milli-Q Synergy Water Purification System, Merck Millipore, MA, USA).

Lyophilized bovine serum albumin (BSA) was purchased from Sigma Life Science (Germany) and dissolved into phosphate buffered saline (PBS, Sigma Life Science) to 100 μM and stored at $4\text{ }^{\circ}\text{C}$. Further dilutions from this stock were prepared in Milli-Q water.

The monoclonal antibody (IgG₁), referred to as mAb, was stored at 11.4 mg/mL in 50 mM citric acid (Acros Organics, Belgium) and 100 mM Tris at pH 7 at $4\text{ }^{\circ}\text{C}$.

The mAb and BSA were labeled with the A488 dye according to the manufacturer's protocol and purified by size exclusion chromatography on a HiTrap desalting column (GE Healthcare, Sweden) and a Superdex 200 10/300 GL (GE Healthcare), respectively.

Polystyrene fluorescent nanoparticles (47 nm average diameter, see size distribution in Figure S1A, Firefli staining dye) were purchased from ThermoFisher Scientific (USA) and diluted to 0.01 ppm in Milli-Q water.

Preparation of Exosomes. Exosomes were isolated from the human bone marrow stromal cell line HS-5 (ATCC, USA) following a procedure similar to a previously described protocol.⁵⁰ Briefly, exosomes were produced from HS-5 cells of 70% confluency cultured for 48 h in Dulbecco's Modified Eagle's Medium (Thermo Fisher Scientific) supplemented with 100 units/mL penicillin (Thermo Fisher Scientific), 100 $\mu\text{g}/\text{mL}$ streptomycin (Thermo Fisher Scientific), 2 mM GlutaMAX (Thermo Fisher Scientific), and 1 mM sodium pyruvate (Thermo Fisher Scientific) under humidified conditions at $37\text{ }^{\circ}\text{C}$ and a 5% CO_2 atmosphere. The cell culture supernatant was clarified by centrifugation at 2,000 and 10,000 $\times g$ at $4\text{ }^{\circ}\text{C}$ using a Sorvall RC 6 PLUS Centrifuge (Thermo Fisher Scientific) equipped with a SA-600 Fixed Angle Rotor (Thermo Fisher Scientific) and filtration through a 0.2- μm pore-sized filter (TPP Techno Plastic Products AG, Switzerland). Exosomes were pelleted at 100,000 $\times g$ for 70 min at $4\text{ }^{\circ}\text{C}$ using an Optima XE-90 (Beckman Coulter Life Sciences, USA) equipped with a Type 45 Ti Fixed-Angle Titanium Rotor (Beckman Coulter Life Sciences) and resuspended in PBS. Exosome size and concentration were characterized by nanoparticle tracking analysis on a ZetaView equipped with a CMOS camera and a 405 nm laser source (Particle Metrix GmbH, Germany). The exosomes were measured at 11 positions with a frame rate of 30 frames/s, a trace length of 15 frames, a gain of 33, and a shutter of 150. The obtained size distribution is shown in Figure S1B. Exosome samples for the DroMiCo were prepared by dilution of the stock sample in Milli-Q water.

Preparation of A β -42 Fibrils. The expression and purification procedures for the peptide A β (M1-42) (MDAEFR-HDSGYEVHHQKLVFFAEDVGSNKGAIIGLMVGGVVIA) were carried out as described previously.^{51,52} In short, A β (M1-42) inclusion bodies were extracted from *E. coli* cells by sonication and dissolved in 8 M urea. Further purification was performed by ion exchange in batch mode on DEAE cellulose

resin with additional lyophilization and gel filtration on a 3.4 cm \times 200 cm gel-filtration column. Fibrils were formed upon A β 42 dilution to 1 μ M in 20 mM sodium phosphate, 0.2 mM EDTA, pH 8.0, and incubation at 37 $^{\circ}$ C. After achieving full conversion, the A β 42 fibrils were sonicated 3 times at 10 s and 40% power on a Bandelin ultrasonic homogenizer SONOPULS HD 2070.2 (Germany) and diluted to the desired concentration in Milli-Q water.

Expression and Purification of Dhh1. mCherry-tagged Dhh1 was expressed and purified as previously described.^{44,45} Briefly, competent *E. coli* BL21-Gold (DE3) strains were transformed via heat shock with an IPTG-inducible plasmid carrying the gene for mCherry-tagged Dhh1, a 6x His tag, and an ampicillin resistance gene (pKW3631). Cells were cultured in LB medium at 37 $^{\circ}$ C until an OD₆₀₀ of 0.7 was reached, and protein expression was induced with 0.5 mM IPTG at 20 $^{\circ}$ C. The cells were harvested by centrifugation, resuspended in lysis buffer (300 mM NaCl, 50 mM Tris, 10 mM imidazole, 10% glycerol, pH 7.5), and lysed by sonication. The protein was purified from the cell extract by affinity chromatography on a Ni²⁺ charged Fast Flow Chelating Sepharose resin (GE Healthcare) followed by size exclusion chromatography on a Superdex 75 column (GE Healthcare) in 300 mM NaCl, 25 mM Tris, 2 mM 2-mercaptoethanol, 10% glycerol, pH 7.5. SDS-PAGE and Coomassie staining were used to test for fraction purity, after which pure fractions were pooled, concentrated to about 200 μ M, and flash-frozen in small aliquots in liquid nitrogen.

Size Exclusion Chromatography (SEC) of BSA. Size exclusion chromatography was performed on an Agilent 1100 series HPLC unit (Santa Clara, CA, USA), equipped with a quaternary pump, an autosampler, a column thermostat, and a UV detector operating at 280 nm. Ten μ g and 0.0001 μ g of BSA-A488 samples were separated on a Superdex 200 10/300 GL, 10 \times 300 mm size exclusion column operating at a flow rate of 0.5 mL/min in PBS. One mL fractions of eluate were collected, dialyzed at room temperature for 4 h in 100 \times diluted PBS, and further analyzed with the DroMiCo.

Phase Diagrams of Lysozyme, PEG, and Dhh1. Solutions of Chicken Egg White Lysozyme (AppliChem, Germany) and NaCl (Fisher Scientific) were prepared at four initial concentrations of (1) 7 mg/mL lysozyme, 0.68 M NaCl, (2) 33 mg/mL lysozyme, 0.60 M NaCl, (3) 24 mg/mL lysozyme, 0.20 M NaCl, and (4) 45 mg/mL lysozyme, 0.20 M NaCl, corresponding to lysozyme:precipitant weight ratios of 0.2, 0.9, 2.0, and 3.9.

PEG 600 (Sigma-Aldrich) and ammonium sulfate (Sigma-Aldrich) were mixed at 3 initial concentrations of (1) 67 mg/mL PEG 600, 8.4 mg/mL (NH₄)₂SO₄, (2) 77 mg/mL PEG 600, 2.0 mg/mL (NH₄)₂SO₄, and (3) 78 mg/mL PEG 600, 0.6 mg/mL (NH₄)₂SO₄, corresponding to PEG:precipitant weight ratios of 8.0, 38.5, and 130.0.

mCherry-Dhh1, ATP, and polyU were mixed according to the following procedure: a stock of 50 mM ATP and 0.2 mg/mL polyU was prepared in 52 mM MgCl₂, 30 mM HEPES-KOH, pH 7.4. The protein mCherry-Dhh1 was diluted to 0.3 μ M in 30 mM HEPES-KOH, 200 mM KCl, 2 mM MgCl₂, pH 7.4. The ATP-polyU stock as well as the protein at 0.3 μ M was then further diluted 10 \times in Milli-Q water and mixed in a 2:1 protein:ATP-polyU v/v ratio. This procedure yielded final concentrations of 1.7 mM ATP, 7 μ g/mL polyU, 0.02 μ M Dhh1, and 13 mM KCl.

Fabrication of the Microfluidic Concentrator Device (DroMiCo). The DroMiCo consisted of a two PDMS layers aligned on top of each other, as described in Figure S2. The first layer, measuring 60 μ m height, contained the main channels with a droplet generation module, in which both the aqueous inlet and the oil inlet channels measured 50 μ m wide, followed by a long 450 μ m wide channel. The second layer consisted of an array of cylindrical traps with diameters of 200 μ m and a depth of 180 μ m. Two corresponding molds, one for each of the described layers, were prepared by spin-coating SU-8 photoresist on silica wafers (MicroChemicals, Germany) (Figure S3). Selected regions of the coated wafers were exposed to UV light for curing. Standard soft-lithography was used to replicate the obtained channels (Figure S4). Polydimethylsiloxane (PDMS, Silicone elastomer 184, Sylgard 184 kit, Dow Corning, USA) mixed with the corresponding cross-linker at a 15:1 weight ratio was cast on the molds and degassed under vacuum at 10 mbar for 30 min. Thick (approximately 10 mm) and thin (<1 mm) PDMS layers were prepared from the master wafers, corresponding to the layers with the channels and the traps, respectively. Partial curing of these PDMS layers was achieved by incubation for 25 min at 70 $^{\circ}$ C. After peeling off the PDMS layers from the wafers, the trap layer was aligned and contact bonded to the channel layer. Full bonding of the two layers and complete curing of the PDMS were achieved by incubating the device at 60 $^{\circ}$ C overnight.

Device Operation. Water-in-oil droplets were generated by emulsifying water solutions in Fluoridrop 7500 oil (Dolomite Microfluidics, United Kingdom) with 0.1% Picosurf 1 (Dolomite Microfluidics) as surfactant. The flow in the channels was imposed with syringe pumps (Cetoni neMESYS, Cetoni GmbH, Germany). The device was initially filled with air, which led to the formation of air bubbles in the traps upon application of flow (Movie S1, in bright field microscopy). These bubbles disappeared over time due to the escape of air through the porous PDMS. This transition time allowed us to discard initial droplets of undesired size, therefore avoiding the need of waste channels and simplifying the design of the device. Monodisperse droplets with sizes compatible with the cylindrical traps were generated and trapped as they traveled along the channel (Movie S1). After trapping the desired number of droplets (typically around 20), the stream containing the analyte was stopped, while a constant flow of the oil phase was maintained at 2 μ L/min to shrink the droplets (Movie S2, in fluorescence microscopy).

Image Acquisition and Analysis. Fluorescence and bright field images were acquired on a Ti2-U epi-fluorescence inverted microscope (Nikon, Switzerland) equipped with an automatic stage, LED light sources operating at 455 nm and 505–600 nm (Omicron Laserage Laserprodukte GmbH, Germany), and a camera (Zyla sCMOS 4.2P-CL10, Andor, United Kingdom). The different analytes were detected with filter cubes sets (AHF Analysentechnik AG, Germany) at the following excitation/emission wavelengths: CFT ET filter set (426–446 nm/460–500 nm, 455 nm beamsplitter) for the exosomes, amyloid fibrils, the protein fluorescence, and the fluorescent nanoparticles, EGFP ET filter set (450–490 nm/500–550 nm, 495 nm beamsplitter) for the A488 fluorophore, and an mCherry filter set (560 nm/635 nm) for the mCherry tagged Dhh1. Droplets were imaged with a water-dipping 60 \times magnification objective (CFI Apo 60XW NIR, Nikon, Switzerland). On this optical setup, typical sample acquisition parameters were 1000 ms exposure time and 100% LED intensity power.

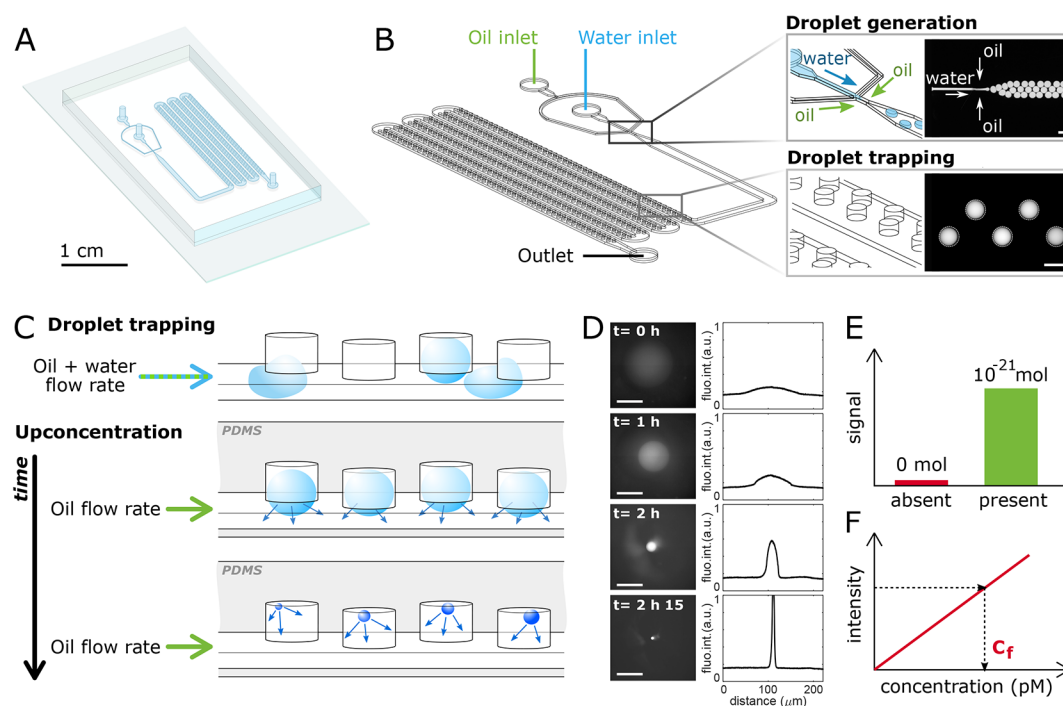


Figure 1. Working principle of the DroMiCo. (A) Illustration of the DroMiCo, consisting of two PDMS layers bonded together and held on a glass coverslip. (B) Schematic diagram of the DroMiCo, which consists of a flow-focusing droplet generation module and a long channel with droplet traps. Corresponding fluorescence images are shown on the right, in which droplets are stained with a fluorophore at high concentration to allow visualization. Scale bar is $200 \mu\text{m}$. (C) Schematic diagram illustrating the droplet concentration process over time. Water from the droplets is extracted by the oil phase, thereby shrinking the aqueous droplets and concentrating their content. (D) Images illustrating the decrease of droplet volume and the corresponding increase of the fluorescence intensity over time. Scale bar is $100 \mu\text{m}$. (E,F) The analysis of the final droplet intensity leads to (E) the detection of trace species present at very low amounts and (F) the accurate quantification of the analyte concentration in the droplets, obtained from a calibration curve relating the final droplet intensity to the droplet final concentration.

The images were analyzed with a home-written MATLAB code (R2016b). Flat field correction was applied to each pixel i to correct for the background of the camera as well as for inhomogeneities in the illumination field (eq 1)

$$I_{\text{corr},i} = \frac{I_{\text{measured},i} - DF_i}{I_{\text{background fit},i}} - 1 \quad (1)$$

where I_{corr} and I_{measured} represent, respectively, the corrected image and the raw measured image; DF is the dark field image subtracted from each sample image; and $I_{\text{background fit}}$ is the background intensity under the droplet, estimated by performing a linear 3D surface fit of a selected donut-shaped region around each droplet (Figure S5). The division of each intensity pixel by the corresponding background value leads to a normalized background value of 1, which is therefore subtracted to give a background value of 0. For each identified droplet, the obtained intensities were integrated in space, yielding the reported values I_{tot} .

The variables measured in each experiment were therefore the initial droplet volume V_0 and the final droplet volume V_f , as well as the droplet final total intensity I_{tot} which reports for the total mass encapsulated in the droplet. The latter was also reported in terms of normalized droplet intensity, I_{tot}/V_0 and I_{tot}/V_f which correspond to the initial and final concentrations in the droplet, respectively.

RESULTS AND DISCUSSION

Principle of the DroMiCo. The DroMiCo consists of a series of modules that are designed to successively generate, trap,

incubate, and detect individual droplets containing the analyte of interest at an undetectable concentration (Figure 1A). First, water-in-oil (W/O) droplets are generated using a flow-focusing geometry, as illustrated in Figure 1B. This configuration allows one to generate and process large numbers of monodisperse droplets (Figure S6), whose size can be easily controlled by changing the channel geometry as well as the volumetric flow rates of the two phases.

The droplets are generated as vertically squeezed objects and get trapped in cylindrical microwells located on top of the channel as they flow past (Figure 1B,C, Movie S1). The trapping of the droplets in the wells is largely driven by surface tension minimization due to the change in aspect ratio from the main channel to the droplet traps,³⁵ which are designed to allow the full relaxation of the droplets into spheres. This spherical 3D shape enables the accurate evaluation of the volume of the initial droplets. Moreover, buoyancy further contributes to the trapping of the droplets in the microwells, as the water droplets are less dense than the oil phase.⁵³ After generating and trapping the droplets, the aqueous flow rate is stopped, while the oil flow rate is kept minimal at $2 \mu\text{L}/\text{min}$ to accelerate droplet shrinking and prevent entrance of air in the device (Figure 1C). An initial bright field image of approximately 20 trapped droplets is acquired to obtain information on their initial volume V_0 .

The droplet shrinkage could be due to either water evaporation through the PDMS or water extraction in the oil. While the first is independent of the position of the trapped droplet, water extraction in the oil depends on the water concentration in the oil, which depends on the position of the droplet trap since the oil saturation increases along the channel

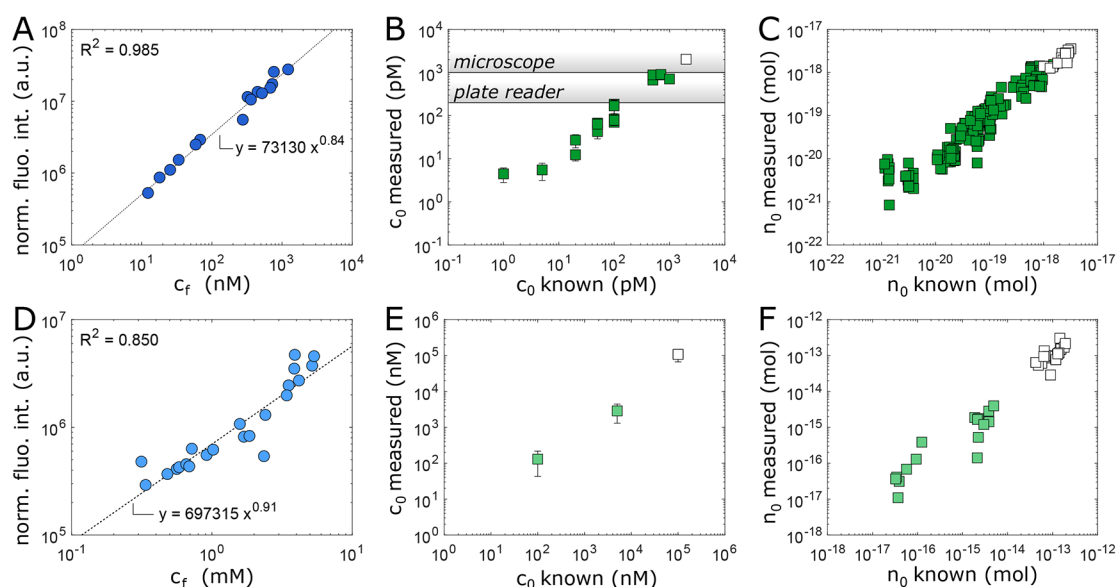


Figure 2. Calibration curves and detection limits of the droplet concentrator device for the dye, A488 (A,B,C), and unlabeled BSA (D,E,F). (A) Calibration curve correlating normalized intensities of individual droplets with analyte concentration, obtained with a standard A488 solution with initial concentrations of 2 nM. The fit (dotted line) is used in B,C) to correlate the measured intensities to the concentrations in the droplet at the end of the shrinking process, from which the initial concentration and amount can be determined using the relationship $C_0 = C_f \times V_f/V_0$, and $n = C_f \times V_f$, respectively. (B) Measured versus known concentrations of different A488 samples. Concentrations as low as 5 pM could be accurately measured, corresponding to (C) zeptomole (10^{-21}) amounts of A488. The detection limits of the microscope and of a conventional plate reader are orders of magnitude higher than the detection limit of DroMiCo. (D) Calibration curve obtained from a sample containing 100 μM of BSA, measured by fluorescence in the visible light range. This plot correlates normalized droplet intensity to final droplet concentration. (E) Measured versus known concentrations of BSA samples, obtained using the fit in panel D). Concentrations as low as 100 nM, corresponding to attomole amounts of BSA, could be accurately measured relying on the fluorescence of BSA, eliminating the need for sample labeling. (F) Measured versus known amount of BSA trapped in the droplets for the respective concentrations investigated in panel E). The white symbols in B,C) and E,F) correspond to the samples used to build the calibration curves in A) and D), respectively. Error bars correspond to the standard deviation of the measurement of 10 to 20 droplets. The results for single droplets are shown in C) and F).

(Figure S7A). We observed that droplets shrink faster when in closer proximity to the oil inlet (Figure S7B,C), indicating that droplet shrinkage occurs by extraction of water molecules from the aqueous droplets to the oil phase (Movie S2). We also observed that the shrinking process significantly slows down once the droplets reach a diameter of around 3 μm , as observed in the literature, which is likely due to thermodynamic contributions⁵⁴ and the high concentration of analytes at the droplet interface⁵⁵ (Figure S7D).

We designed the geometry of the traps to leverage buoyancy and ensure that the droplets remain trapped in the chambers even upon severe shrinkage, thereby enabling us to image their contents over time (Figure 1C). The size of the trapped droplets is monitored by bright field optical microscopy during the shrinkage process (Figure 1D). Once the diameter of the droplet is reduced below 20 μm , a final fluorescent image is acquired to measure the volume V_f and intensity I_{tot} of the droplet. Droplets are imaged only once in fluorescence mode to avoid fluorophore bleaching upon repetitive exposure.

By measuring standard polymeric nanoparticles of known size, we estimate that the smallest dimension of a droplet that can be accurately measured with our optic system is 2 μm (Figure S8). The largest diameter of spherical droplets generated in this study was 200 μm . Therefore, the maximal achievable concentration factor with this current device design is theoretically 1,000,000-fold. This ratio represents the upper theoretical limit of the technique, and we typically reached a concentration factor of 100,000 \times , which could be further

optimized by improving the sensitivity of the detection method or by generating larger initial droplets.

The shrinking droplet concentrator device (DroMiCo) is particularly well-suited for two applications: the detection of trace amounts of species in solution (Figure 1E) and the accurate quantification of low amounts of analytes in solution (Figure 1F). To enable such quantification, a calibration run is initially performed to correlate droplet intensity with analyte mass. The unknown concentration of the initial droplets is then quantified in a two-step process. First, the concentration of the analyte in the shrunken droplets (C_f) is measured by integrating the recorded intensity signal I_{tot} and comparing this value to the calibration curve. Second, C_f is combined with the known initial and final volume of the droplets (V_0 , V_f) to provide the initially unknown concentration of the analyte $C_0 = C_f \times V_f/V_0$.

In this study, we demonstrate the power of this approach with epi-fluorescence detection, which offers relatively high detection sensitivity. However, the generic principle of the technique is independent of the specific detection method.

Detection of Zeptomole Amounts of Analytes. We first explored the detection limits of the DroMiCo with the fluorescent dye Atto-Tec 488 (A488), which exhibits high photostability and retention in water-in-oil droplets.⁵⁶ A calibration curve was initially generated by measuring a sample at 2 nM, corresponding to the lower limit of the concentration range that can be detected by the microscope (Figure 2A). This calibration allows one to correlate the analyte concentration in the droplet to the normalized droplet intensity, which is

calculated by dividing the integrated droplet intensity by the final volume of the droplet.

We then measured samples containing different concentrations of A488 and compared the values obtained with the expected concentrations (Figure 2B). We observed good agreement between measured and expected values with concentrations as low as 5 pM. This value corresponds to an average of 3000 fluorophore molecules within individual droplets, equal to 5 zeptomole (zmol, 10^{-21} mol, Figure 2C). Repetitions of independent samples demonstrated the good reproducibility of the assay (Figure S9). This concentration is several orders of magnitude lower than the detection limit of conventional tools used in common biochemical assays. For instance, we estimated the detection limit of conventional plate readers and standard epi-fluorescence microscopes to be approximately hundreds of pM and 1 nM, respectively (Figure 2B, droplet at time 0 h). The detection limit of the DroMiCo in the pM range is similar to other advanced microfluidic platforms, such as the recently developed droplet-based sample chopper, which is compatible with both absorbance and fluorescence detection.^{57,58}

To demonstrate the compatibility of the DroMiCo with various detection methods, we investigated its potential to detect low amounts of proteins based on their fluorescence in the visible light range. As model analyte, we used unlabeled BSA (Figure S10A). Following the same procedure described above, we first generated a calibration curve with a sample containing 100 μ M of BSA (Figure 2D). We then measured a series of diluted samples, achieving an excellent agreement between measured and expected values down to 100 nM (Figure 2E,F). This measurement outperforms other conventional assays, such as the bicinchoninic acid (BCA) or Bradford assays by at least 1 order of magnitude.^{42,43}

The sensitivity of our droplet microfluidic approach is limited by potential challenges, including the quantum yield of the fluorophore, the transport of the molecules from the droplets to the continuous oil phase during incubation, the interactions of the molecules with the surfactant stabilizing the droplets, and high background values in the case of samples containing fluorescent impurities. The hydrophobicity of the carrier oil is also an important factor. The solubility of water into the oil should be sufficiently high to allow droplet shrinkage in a reasonable time scale, but excessive oil hydrophilicity could promote leakage of water-soluble components by diffusion into the oil. Moreover, photobleaching could occur with epi-fluorescence detection. Currently, these limitations decrease the maximal concentration factor which could be achievable with this technique and may alter its accuracy. These limitations can be alleviated in the future by accelerating the shrinkage process, for instance by application of osmotic pressure, by optimizing the chemistry of the components of the emulsion, such as the oil phase, and by increasing the sensitivity of imaging techniques. The total duration of the experiment is 4–5 h and includes mainly the shrinking of the droplets. The number of monitored replicate droplets was selected based on our chip design to optimize the amount of information while minimizing the experimental time (Figure S7).

The DroMiCo as Generic Detection Tool. We next demonstrated the generic applicability of the DroMiCo to a broad range of target analytes in simple buffers. We considered the small molecule A488 at 20 pM, a labeled antibody sample (mAb-A488 conjugated) at 5 pM, fluorescent polymeric nanoparticles at 0.01 ppm (2000 part./nL), unlabeled exosomes

at 10^7 part./mL (10 part./nL, which corresponds to approximately 10 part./droplet), and unlabeled amyloid fibrils of the peptide A β 42 at 1 pM. Exosomes and amyloid fibrils were detected based on the fluorescence in the visible light range (in the case of exosomes originating from the proteins contained in these vesicles). This fluorescence signal of proteins in the deep blue spectrum (approximately 450 nm) has been observed in the literature, although its origin has not been clarified yet.^{59–61} A Milli-Q water sample was measured as reference background for all samples, using the same fluorescence wavelengths of the samples (436 nm/480 nm for fluorescent nanoparticles, exosomes, and A β 42 fibrils, and 470 nm/525 nm for the A488 and mAb-A488). In all measured samples, we detected a fluorescent signal significantly larger than the background value, indicating the presence of the target analyte (Figure 3).

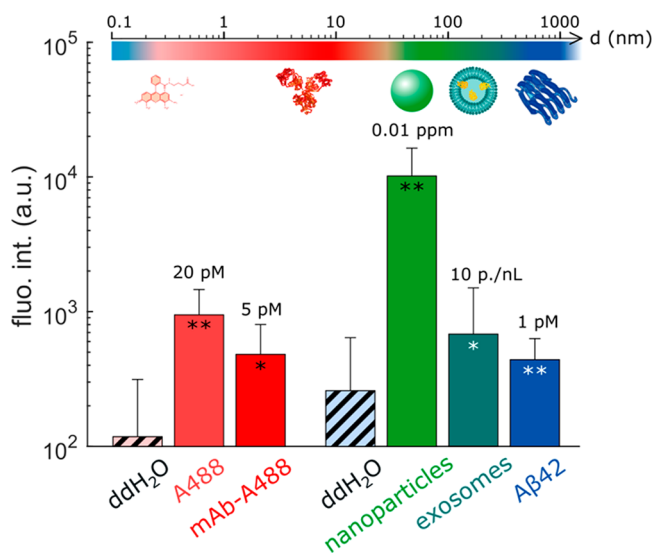


Figure 3. The DroMiCo is able to detect the presence of minute amounts of analyte, as shown with the dye A488 at 20 pM, the labeled antibody at 5 pM, fluorescent nanoparticles at concentrations of 0.01 ppm (2000 part./nL), unlabeled exosomes at 10 part./nL, and unlabeled A β 42 at 1 pM. The respective control samples with only Milli-Q water (ddH₂O) are shown with striped bars. Error bars correspond to the standard deviation of 10 to 20 droplets. Statistical unpaired *t*-tests result in *p*-values <0.05 (*) and <10⁻² (**).

These results demonstrate that the proposed strategy represents a simple approach to increase the concentration of molecules spanning a broad range of sizes from a few angstroms to several hundreds of nanometers, independent of their specific physicochemical properties. This ability is especially useful to quantify analytes whose signal cannot be amplified, due to a lack of knowledge on the analyte structural properties, or sample heterogeneity, as shown here with the nanoparticles, protein aggregates, and exosomes.

Prefractionation and Detection with the DroMiCo.

After illustrating the concept of the microfluidic droplet concentrator with individual analytes, we next demonstrate a potential application of the DroMiCo for the detection of individual target species isolated from multicomponent mixtures. Chromatography, such as size exclusion chromatography (SEC), is commonly applied for the separation of biomolecules and their complexes. However, in some cases the concentration of the target analyte may be lower than the detection limit of conventional spectrophotometry. In this case,

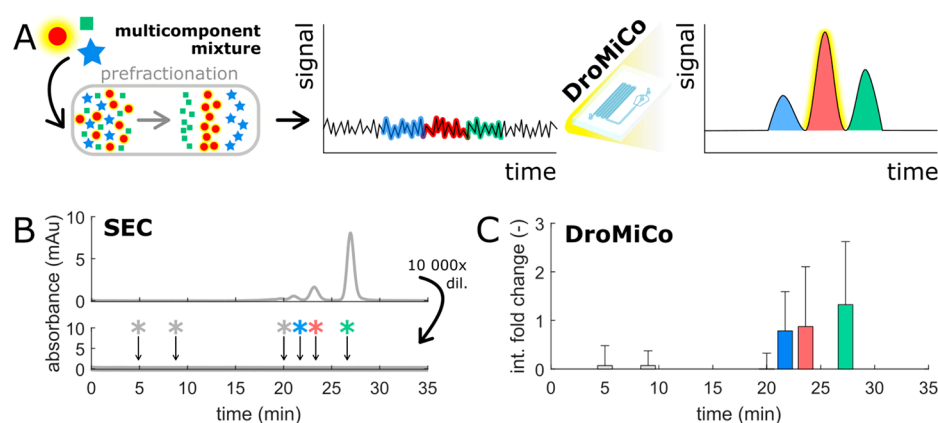


Figure 4. A) A prefractionation step coupled with the DroMiCo allows the separation and detection of small amounts of specific analytes in solution, typically undetectable with classical detection techniques. B) We illustrate this concept by detecting small amounts of BSA oligomers labeled with A488. UV absorbance chromatogram obtained after injection of 10 μg of BSA-A488 (top) and 100 pg of BSA-A488 (bottom). The peaks in the SEC chromatogram in the upper graph correspond to different protein species: from right to left, monomer, dimer, trimer, and higher order oligomers. The UV detector displays a flat absorbance signal for the 100 pg BSA-A488 sample (lower graph). The marked regions (*) correspond to fractions analyzed with the DroMiCo. C) In contrast, the microfluidic droplet concentrator is able to reconstruct the signal of the different fractions collected in the bottom chromatogram in B). The bars represent the intensities of monomer (green), dimer (red), and trimer (blue) normalized to the average of the background fractions (gray). Error bars correspond to the standard deviation of 10 to 20 droplets.

the chromatogram could be reconstituted by measuring the individual separated fractions by the DroMiCo (Figure 4A). We illustrate this concept by separating undetectable target protein oligomers in a BSA solution by SEC. These oligomeric species formed spontaneously in a solution of 1 mg/mL BSA labeled with the A488 dye (BSA-A488). We injected 10 μg into a SEC column and fractionated the oligomeric mixture of BSA into the individual monomer, dimer, trimer, and higher order species (see insert Figure 4B). Upon 10,000-fold dilution of this sample and injection of 100 pg of labeled BSA, no protein signal could be detected by conventional online UV absorbance (Figure 4B). In contrast, measurement with the DroMiCo allowed us to reconstruct the expected chromatogram and detect the picogram amounts of labeled BSA oligomers injected into the column (Figure 4C).

Phase Behavior of Macromolecules for an *in Vitro* Model of Membraneless Cellular Compartments. The increase in concentration of macromolecules in solution often leads to phase separation phenomena such as liquid–solid and liquid–liquid phase separation. Based on its ability to selectively extract water from the solution, the DroMiCo is an ideal platform to investigate the phase behavior of macromolecules and evaluate the impact of molecular modulators on their phase separation.

We first illustrate this concept with a solution containing lysozyme at five different lysozyme/precipitant (NaCl) weight ratios, varying in the range from 0.2 to 3.9. Upon concentration of the protein within the droplets in the DroMiCo, we were able to identify the liquid–solid phase boundary of the system (Figure 5). For each condition, this boundary was observed at protein and salt concentrations that were consistent for all the different replicate droplets. Importantly, the phase diagram at high protein concentrations was obtained starting from dilute solutions that required only a few tens of μg of protein per investigated condition.

An additional advantage of the DroMiCo is the ability to observe the phase separation and identify crystalline, solid, or liquid phases. For instance, by investigating the phase diagram of mixtures of PEG 600 and ammonium sulfate, we were able to identify a first phase boundary between a homogeneous liquid

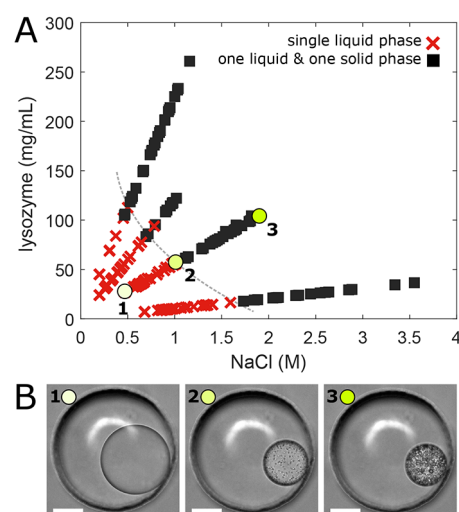


Figure 5. A) Phase diagram for the lysozyme–NaCl mixture obtained with the DroMiCo. The dotted line is a guide for the eye representing the phase boundary. For each of the four conditions 20 replicate droplets were analyzed. B) Images of one droplet undergoing the concentration process in the DroMiCo at different time points, as shown in the corresponding points in the phase diagram in A). Scale bar is 50 μm.

solution and two coexisting liquid phases, as well as a second phase boundary corresponding to precipitation of ammonium sulfate (Figure 6).

Finally, we applied the DroMiCo to investigate the phase diagram of a more complex system that represents an *in vitro* model of cellular membraneless compartments, which have recently gained interest due to their role in a variety of cellular processes.^{46–48} Many fundamental aspects underlying the formation of these compartments still remain elusive, including the dynamics of their assembly and disassembly.^{45,48,49} Here, we analyzed an established model of processing bodies (P-bodies) consisting of the DEAD-box protein ATPase Dhh1, which undergoes phase separation in the presence of ATP and polyU, an RNA analog (Figure 7A).^{44,45} We encapsulated homoge-

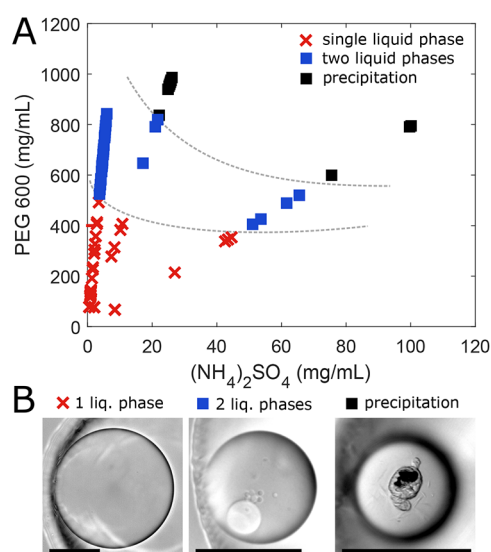


Figure 6. A) Phase diagram obtained with the DroMiCo for the PEG–ammonium sulfate mixtures. The dotted lines are guides for the eye representing the phase boundaries. B) Images of droplets undergoing the concentration process in the DroMiCo at different time points, corresponding to different points in the phase diagram in A). Scale bar is 50 μm .

neous solutions of Dhh1, ATP, and polyU at concentrations under which no phase separation is observed, namely 0.02 μM Dhh1, 1.7 mM ATP, and 0.007 mg/mL polyU. Upon removal of water from the mixture, the concentration of all components increased until liquid–liquid phase separation (LLPS) was observed (Figure 7B–C). The liquid-like properties of the protein-rich phase were confirmed by the observation of merging events between the condensates until one single spherical droplet was formed (Figure 7D). These results demonstrate that the shrinking process in the DroMiCo allows investigating protein phase diagrams at increasing protein concentrations starting from homogeneous solutions at subcritical concentrations. This allows to mimic biological phase transition upon volume loss⁶² or local increase in RNA and protein concentration⁶³ induced by cellular stresses. A significant advantage of the DroMiCo is its ability to observe the

phase separation in real time upon increasing the protein concentration. Furthermore, this technique allows one to explore a broad range of concentrations including high concentrations of biomolecules that are typically inaccessible in bulk assays, while only requiring minute amounts of material (on the order of hundreds of micrograms).

CONCLUSION

We developed a microfluidic droplet platform able to concentrate trace compounds in simple solutions by decreasing sample volume under well-defined conditions. This technique facilitates the detection of a wide range of target analytes with optical methods, without requiring any *a priori* information on the structure nor physical-chemical properties of the analyte. This feature is particularly relevant for the detection of bioanalytes with poorly defined structures or analytes that cannot be amplified.

We have demonstrated the power of this approach with a broad range of analytes from a few angstroms to hundreds of nm in size, including small molecules, proteins, nanoparticles, exosomes, and amyloid fibrils. We showed that the DroMiCo can quantify trace amounts of a model analyte down to 5 pM. Moreover, we demonstrated that this device can measure concentrations of unlabeled proteins with a sensitivity increase of 1 order of magnitude over conventional methods. Overall, our concentration technique represents a powerful tool for analyte detection and quantification which can be implemented for pre-concentration steps or coupled with other assays to enhance signal specificity. Other potential applications include the analysis of binding events or single-step immunoassays based for instance on FRET detection or any other fluorophore/quencher pair.

We have further demonstrated the applicability of the DroMiCo in the analysis of phase diagrams of macromolecules, based on its ability to remove water molecules and span a broad range of concentrations due to the high concentration factor of approximately 100,000-fold. A significant advantage of the DroMiCo is the ability to observe the state of the dispersed phase and differentiate processes such as precipitation, crystallization, and liquid–liquid phase separation. We illustrated these concepts starting from a simple solution of lysozyme and NaCl undergoing liquid–solid phase transition, as well as a

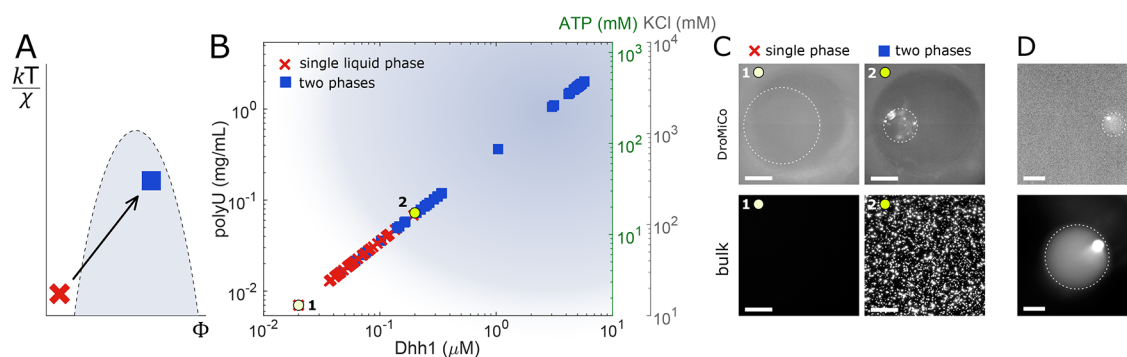


Figure 7. A) Schematic illustration of the phase diagram of the DEAD-box protein ATPase Dhh1, which is controlled by two molecular modulators, ATP and polyU. Cross and square indicate absence and presence of phase separation, respectively. B) Phase diagram obtained with Dhh1 in the presence of ATP and polyU, starting with a homogeneous solution of 0.02 μM Dhh1, 1.7 mM ATP, and 0.007 mg/mL polyU. C) Fluorescence images of one droplet at time 0 h and after liquid–liquid phase separation and corresponding controls in bulk. Scale bar is 50 μm . D) Dhh1-rich condensates merge into one single droplet, demonstrating their liquid-like nature. Starting conditions were as follows: 0.02 μM Dhh1, 1.7 mM ATP, and 0.007 mg/mL polyU (top, concentration factor of 233) and 0.3 μM Dhh1, 1.7 mM ATP, and 0.007 mg/mL polyU (bottom, concentration factor of 56). Scale bar is 10 μm .

solution of PEG and ammonium sulfate undergoing LLPS followed by precipitation. In addition, the DroMiCo was applied to a more complex system consisting of an *in vitro* model of cellular membraneless organelles, demonstrating its ability to mimic biological phase separation induced for instance by volume loss or by increase of RNA and protein concentration upon stresses. Furthermore, the technique can operate at high concentration ranges that are typically inaccessible in bulk assays, while using minute amounts of sample.

■ ASSOCIATED CONTENT

Supporting Information

The Supporting Information is available free of charge at <https://pubs.acs.org/doi/10.1021/acs.analchem.9b05329>.

Size distributions of analytes; microfluidic device design and fabrication; data analysis; position dependent droplet shrinking behavior; reproducibility; and unlabeled protein fluorescence spectra (PDF)

Movie S1 (AVI)

Movie S2 (AVI)

■ AUTHOR INFORMATION

Corresponding Author

Paolo Arosio – Department of Chemistry and Applied Biosciences, Institute for Chemical and Bioengineering, ETH Zurich, Zurich 8093, Switzerland; orcid.org/0000-0002-2740-1205; Email: paolo.arosio@chem.ethz.ch

Authors

Marie R. G. Kopp – Department of Chemistry and Applied Biosciences, Institute for Chemical and Bioengineering, ETH Zurich, Zurich 8093, Switzerland

Miriam Linsenmeier – Department of Chemistry and Applied Biosciences, Institute for Chemical and Bioengineering, ETH Zurich, Zurich 8093, Switzerland

Britta Hettich – Department of Chemistry and Applied Biosciences, Institute of Pharmaceutical Sciences, ETH Zurich, Zurich 8093, Switzerland

Sebastian Prantl – Department of Chemistry and Applied Biosciences, Institute for Chemical and Bioengineering, ETH Zurich, Zurich 8093, Switzerland

Stavros Stavarakis – Department of Chemistry and Applied Biosciences, Institute for Chemical and Bioengineering, ETH Zurich, Zurich 8093, Switzerland; orcid.org/0000-0002-0888-5953

Jean-Christophe Leroux – Department of Chemistry and Applied Biosciences, Institute of Pharmaceutical Sciences, ETH Zurich, Zurich 8093, Switzerland

Complete contact information is available at:

<https://pubs.acs.org/doi/10.1021/acs.analchem.9b05329>

Notes

The authors declare no competing financial interest.

■ ACKNOWLEDGMENTS

We kindly acknowledge Dr. Lenka Faltova for providing the A β 42 peptide, Yannick Kurz for support in the experiments, and Dr. Tianjin Yang for helpful discussions. We gratefully acknowledge financial support from the ETH Research Grants ETH-33 17-2 and ETH-10 16-1, the Synapsis Foundation for Alzheimer's Disease, and the Swiss National Science Foundation (grant 205321_179055).

■ REFERENCES

- (1) Benilova, I.; Karran, E.; De Strooper, B. *Nat. Neurosci.* **2012**, *15*, 349.
- (2) Ono, K.; Condron, M. M.; Teplow, D. B. *Proc. Natl. Acad. Sci. U. S. A.* **2009**, *106* (35), 14745.
- (3) Walsh, D. M.; Selkoe, D. J. *J. Neurochem.* **2007**, *101* (5), 1172–1184.
- (4) Haass, C.; Selkoe, D. J. *Nat. Rev. Mol. Cell Biol.* **2007**, *8*, 101.
- (5) Théry, C.; Zitvogel, L.; Amigorena, S. *Nat. Rev. Immunol.* **2002**, *2* (8), 569–579.
- (6) Van Der Pol, E.; Hoekstra, A. G.; Sturk, A.; Otto, C.; Van Leeuwen, T. G.; Nieuwland, R. J. *Thromb. Haemostasis* **2010**, *8* (12), 2596–2607.
- (7) Walt, D. R. *Anal. Chem.* **2013**, *85* (3), 1258–1263.
- (8) Zhu, Y.; Fang, Q. *Anal. Chim. Acta* **2013**, *787*, 24–35.
- (9) Reyes, D. R.; Iossifidis, D.; Auroux, P.-A.; Manz, A. *Anal. Chem.* **2002**, *74* (12), 2623–2636.
- (10) Auroux, P.-A.; Iossifidis, D.; Reyes, D. R.; Manz, A. *Anal. Chem.* **2002**, *74* (12), 2637–2652.
- (11) Giordano, B. C.; Burgi, D. S.; Hart, S. J.; Terray, A. *Anal. Chim. Acta* **2012**, *718*, 11–24.
- (12) Kopp, M. R. G.; Arosio, P. *J. Pharm. Sci.* **2018**, *107* (5), 1228–1236.
- (13) Charmet, J.; Arosio, P.; Knowles, T. P. J. *J. Mol. Biol.* **2018**, *430* (5), 565–580.
- (14) Duncombe, T. A.; Tentori, A. M.; Herr, A. E. *Nat. Rev. Mol. Cell Biol.* **2015**, *16*, 554.
- (15) Wang, F.; Dong, J.; Jiang, X.; Ye, M.; Zou, H. *Anal. Chem.* **2007**, *79* (17), 6599–6606.
- (16) Hatch, A. V.; Herr, A. E.; Throckmorton, D. J.; Brennan, J. S.; Singh, A. K. *Anal. Chem.* **2006**, *78* (14), 4976–4984.
- (17) Duncombe, T. A.; Herr, A. E. *Lab Chip* **2013**, *13* (11), 2115–2123.
- (18) Lee, J. H.; Cosgrove, B. D.; Lauffenburger, D. A.; Han, J. *J. Am. Chem. Soc.* **2009**, *131* (30), 10340–10341.
- (19) Wang, Y.-C.; Stevens, A. L.; Han, J. *Anal. Chem.* **2005**, *77* (14), 4293–4299.
- (20) Kim, S. M.; Burns, M. A.; Hasselbrink, E. F. *Anal. Chem.* **2006**, *78* (14), 4779–4785.
- (21) Lee, J. H.; Chung, S.; Kim, S. J.; Han, J. *Anal. Chem.* **2007**, *79* (17), 6868–6873.
- (22) Shen, M.; Yang, H.; Sivagnanam, V.; Gijs, M. A. M. *Anal. Chem.* **2010**, *82* (24), 9989–9997.
- (23) Mao, Z.; Li, P.; Wu, M.; Bachman, H.; Mesyngier, N.; Guo, X.; Liu, S.; Costanzo, F.; Huang, T. J. *ACS Nano* **2017**, *11* (1), 603–612.
- (24) Huang, L. R.; Cox, E. C.; Austin, R. H.; Sturm, J. C. *Science* **2004**, *304* (5673), 987.
- (25) Foote, R. S.; Khandurina, J.; Jacobson, S. C.; Ramsey, J. M. *Anal. Chem.* **2005**, *77* (1), 57–63.
- (26) Lee, J. H.; Song, Y.-A.; Tannenbaum, S. R.; Han, J. *Anal. Chem.* **2008**, *80* (9), 3198–3204.
- (27) Krivitsky, V.; Hsiung, L.-C.; Lichtenstein, A.; Brudnik, B.; Kantaev, R.; Elnathan, R.; Pevzner, A.; Khatchourint, A.; Patolsky, F. *Nano Lett.* **2012**, *12* (9), 4748–4756.
- (28) Yu, C.; Davey, M. H.; Svec, F.; Fréchet, J. M. J. *Anal. Chem.* **2001**, *73* (21), 5088–5096.
- (29) Tang, M. Y. H.; Shum, H. C. *Lab Chip* **2016**, *16* (22), 4359–4365.
- (30) Svec, F. *J. Chromatogr. B: Anal. Technol. Biomed. Life Sci.* **2006**, *841* (1), 52–64.
- (31) Chen, C.-H.; Sarkar, A.; Song, Y.-A.; Miller, M. A.; Kim, S. J.; Griffith, L. G.; Lauffenburger, D. A.; Han, J. *J. Am. Chem. Soc.* **2011**, *133* (27), 10368–10371.
- (32) Horrocks, M. H.; Tosatto, L.; Dear, A. J.; Garcia, G. A.; Iljina, M.; Cremades, N.; Dalla Serra, M.; Knowles, T. P. J.; Dobson, C. M.; Klenerman, D. *Anal. Chem.* **2015**, *87* (17), 8818–8826.
- (33) Pfammatter, M.; Andreassen, M.; Meisl, G.; Taylor, C. G.; Adamcik, J.; Bolisetty, S.; Sánchez-Ferrer, A.; Klenerman, D.; Dobson,

- C. M.; Mezzenga, R.; Knowles, T. P. J.; Aguzzi, A.; Hornemann, S. *Anal. Chem.* **2017**, *89* (22), 12306–12313.
- (34) Casadevall i Solvas, X.; Turek, V.; Prodromakis, T.; Edel, J. B. *Lab Chip* **2012**, *12* (20), 4049–4054.
- (35) Shim, J.-u.; Cristobal, G.; Link, D. R.; Thorsen, T.; Jia, Y.; Piattelli, K.; Fraden, S. *J. Am. Chem. Soc.* **2007**, *129* (28), 8825–8835.
- (36) Fornells, E.; Hilder, E. F.; Breadmore, M. C. *Anal. Bioanal. Chem.* **2019**, *411* (9), 1715–1727.
- (37) Walker, G. M.; Beebe, D. J. *Lab Chip* **2002**, *2* (2), 57–61.
- (38) Bleier, B. J.; Anna, S. L.; Walker, L. M. *J. Phys. Chem. B* **2018**, *122* (14), 4067–4076.
- (39) Garcia-Cordero, J. L.; Fan, Z. H. *Lab Chip* **2017**, *17* (13), 2150–2166.
- (40) Mampallil, D.; Tiwari, D.; van den Ende, D.; Mugele, F. *Biomicrofluidics* **2013**, *7* (4), No. 044102.
- (41) He, M.; Sun, C.; Chiu, D. T. *Anal. Chem.* **2004**, *76* (5), 1222–1227.
- (42) Smith, P. K.; Krohn, R. I.; Hermanson, G. T.; Mallia, A. K.; Gartner, F. H.; Provenzano, M. D.; Fujimoto, E. K.; Goeke, N. M.; Olson, B. J.; Klenk, D. C. *Anal. Biochem.* **1985**, *150* (1), 76–85.
- (43) Bradford, M. M. *Anal. Biochem.* **1976**, *72* (1), 248–254.
- (44) Mugler, C. F.; Hondele, M.; Heinrich, S.; Sachdev, R.; Vallotton, P.; Koek, A. Y.; Chan, L. Y.; Weis, K. *eLife* **2016**, *5*, No. e18746.
- (45) Linsenmeier, M.; Kopp, M. R. G.; Grigolato, F.; Emmanouilidis, L.; Liu, D.; Zürcher, D.; Hondele, M.; Weis, K.; Capasso Palmiero, U.; Arosio, P. *Angew. Chem., Int. Ed.* **2019**, *58* (41), 14489–14494.
- (46) Brangwynne, C. P.; Eckmann, C. R.; Courson, D. S.; Rybarska, A.; Hoegge, C.; Gharakhani, J.; Jülicher, F.; Hyman, A. A. *Science* **2009**, *324* (5935), 1729.
- (47) Kato, M.; Han, T. W.; Xie, S.; Shi, K.; Du, X.; Leeju, C.; Wu, H.; Mirzaei, E. J.; Goldsmith, J.; Longgood, J. P.; Grishin, N. V.; Frantz, D. E.; Schneider, J. W.; Chen, S.; Li, L.; Sawaya, M. R.; Eisenberg, D.; Tycko, R.; McKnight, S. L. *Cell* **2012**, *149* (4), 753–767.
- (48) Banani, S. F.; Lee, H. O.; Hyman, A. A.; Rosen, M. K. *Nat. Rev. Mol. Cell Biol.* **2017**, *18* (5), 285–298.
- (49) Berry, J.; Weber, S. C.; Vaidya, N.; Haataja, M.; Brangwynne, C. P. *Proc. Natl. Acad. Sci. U. S. A.* **2015**, *112* (38), No. E5237.
- (50) Théry, C.; Amigorena, S.; Raposo, G.; Clayton, A. *Current Protocols in Cell Biology* **2006**, *30* (1), 3.22.1–3.22.29.
- (51) Walsh, D. M.; Thulin, E.; Minogue, A. M.; Gustavsson, N.; Pang, E.; Teplow, D. B.; Linse, S. *FEBS J.* **2009**, *276* (5), 1266–1281.
- (52) Arosio, P.; Michaels, T. C. T.; Linse, S.; Månsson, C.; Emanuelsson, C.; Presto, J.; Johansson, J.; Vendruscolo, M.; Dobson, C. M.; Knowles, T. P. J. *Nat. Commun.* **2016**, *7*, 10948.
- (53) Labanieh, L.; Nguyen, N. T.; Zhao, W.; Kang, D.-K. *Micro-machines* **2015**, *6* (10), 1469.
- (54) Eslami, F.; Elliott, J. A. W. *J. Phys. Chem. B* **2013**, *117* (7), 2205–2214.
- (55) Jeffries, G. D. M.; Kuo, J. S.; Chiu, D. T. *Angew. Chem., Int. Ed.* **2007**, *46* (8), 1326–1328.
- (56) Janiesch, J.-W.; Weiss, M.; Kannenberg, G.; Hannabuss, J.; Surrey, T.; Platzman, I.; Spatz, J. P. *Anal. Chem.* **2015**, *87* (4), 2063–2067.
- (57) Li, X.; Hu, J.; Easley, C. J. *Lab Chip* **2018**, *18* (19), 2926–2935.
- (58) Negou, J. T.; Avila, L. A.; Li, X.; Hagos, T. M.; Easley, C. J. *Anal. Chem.* **2017**, *89* (11), 6153–6159.
- (59) Chan, F. T. S.; Kaminski Schierle, G. S.; Kumita, J. R.; Bertoncini, C. W.; Dobson, C. M.; Kaminski, C. F. *Analyst* **2013**, *138* (7), 2156–2162.
- (60) Wang, Q.; Dou, X.; Chen, X.; Zhao, Z.; Wang, S.; Wang, Y.; Sui, K.; Tan, Y.; Gong, Y.; Zhang, Y.; Yuan, W. *Z. Angew. Chem., Int. Ed.* **2019**, *58* (36), 12667–12673.
- (61) Niyangoda, C.; Miti, T.; Breydo, L.; Uversky, V.; Muschol, M. *PLoS One* **2017**, *12* (5), No. e0176983.
- (62) Joyner, R. P.; Tang, J. H.; Helenius, J.; Dultz, E.; Brune, C.; Holt, L. J.; Huet, S.; Müller, D. J.; Weis, K. *eLife* **2016**, *5*, No. e09376.
- (63) Sachdev, R.; Hondele, M.; Linsenmeier, M.; Vallotton, P.; Mugler, C. F.; Arosio, P.; Weis, K. *eLife* **2019**, *8*, No. e41415.